



Power Electronic Systems  
Laboratory

© 2019 IET

IET Electrical Systems in Transportation, pp. 1-9, January 2019

## **Non-Invasive KERS Based Auxiliary Energy Supply System for Freight Trains**

M. Flankl,  
A. Tüysüz,  
I. Subotic,  
J. W. Kolar,  
Y. Tsukada,  
K. Nakamura

This paper is a postprint of a paper submitted to and accepted for publication in IET Electrical Systems in Transportation and is subject to Institution of Engineering and Technology Copyright. The copy of record is available at the IET Digital Library.



Eidgenössische Technische Hochschule Zürich  
Swiss Federal Institute of Technology Zurich

# Non-invasive KERS-based auxiliary energy supply system for freight trains

 ISSN 2042-9738  
 Received on 18th April 2018  
 Revised 17th October 2018  
 Accepted on 22nd January 2019  
 E-First on 25th February 2019  
 doi: 10.1049/iet-est.2018.5014  
 www.ietdl.org

Michael Flankl<sup>1</sup> ✉, Arda Tüysüz<sup>1</sup>, Ivan Subotic<sup>2</sup>, Johann Walter Kolar<sup>1</sup>, Yusuke Tsukada<sup>3</sup>, Kazuhito Nakamura<sup>3</sup>

<sup>1</sup>Power Electronic Systems Laboratory, Swiss Federal Institute of Technology (ETH), Zurich 8092, Switzerland

<sup>2</sup>Electric Machines and Drives Group, Liverpool John Moores University, Liverpool, L3 3AF England, UK

<sup>3</sup>NABTESCO R&D Centre, Nabtesco Corporation Japan, Kyoto 600-8899, Japan

✉ E-mail: flankl@em.ee.ethz.ch

**Abstract:** Freight wagons typically do not have an electrical train supply and state-of-the-art auxiliary energy generation systems as, e.g. axle generators on freight wagons lack the possibility for a cost-effective retrofit. However, emerging applications, as, e.g. anti-lock braking systems for freight trains or condition monitoring systems for the loaded goods, require electric power in the watt range. Therefore, a non-invasive auxiliary energy supply system with 22 W/dm<sup>3</sup> (360 mW/in<sup>3</sup>) based on a non-coaxial eddy-current coupling is described and analysed in this study. It is a kinetic energy recovery system, which can extract power directly from the motion of a freight wagon's wheel. An air gap of 10 mm between the wheel and a permanent magnet rotor is set during operation, making the system a non-invasive one. A model for the transfer efficiency of the system is established and verified by measurements. The prototype including an optimised generator and an integrated active rectifier for generating a DC-output voltage is built and an electric power of 8 W can be extracted from a steel wheel moving with a surface speed of 22 m/s.

## 1 Introduction

Typically, the wagons of a freight train do not have an electrical train supply, which is in contrast to passenger coaches, where such a supply is used for coach lighting and heating [1]. Emerging applications, which, however, require an electric-power supply are an anti-lock braking system for the freight wagon and condition monitoring of the transported goods. It has the potential of saving costs and giving additional benefit to the freight wagon's operator. Owing to the lack of a non-invasive, easy to install the power supply, the current market penetration of anti-lock braking or condition monitoring systems for freight trains is negligible. One approach to providing electric power would be to utilise a compressed-air-to-electric-power generation system as described in [2]. It could be supplied by the freight train's brake pipe, which delivers compressed air to the braking system. However, such an auxiliary power generation system would then be connected to a safety critical installation (i.e. main brake pipe). Hence, it could lead to an extensive certification process and/or require a redesign of the compressed-air supply system. Furthermore, such a system is obviously not compatible with a vacuum brake.

Providing auxiliary power on a freight train wagon with a conversion from kinetic energy is considered to be a more acceptable approach. A generator attached to the end of the axle, a generator coupled to the rotating axle with a belt drive or a generator coupled with a transmission shaft are well-known approaches; therefore [3]. However, due to their nature, those systems are bulky and difficult/expensive to install in a retrofitting process. Hence, an alternative approach for energy generation, which does not need a sophisticated mounting infrastructure, is required.

Kinetic energy in the form of vibration could be considered as a power source as high amplitudes of ambient vibration are present on a wagon. Typical power levels of vibration-based energy harvesting (EH) systems, presented in the literatures [4, 5] and in the commercial sector [6], achieve only output power levels in the milliwatt range. An approximate power density of 6 mW/dm<sup>3</sup>...1.3 W/dm<sup>3</sup> (100W/in<sup>3</sup>...21mW/in<sup>3</sup>), depending on

the amplitude and frequency of the vibration was reported. However, due to material cost and mounting constraints, a power density of >10 W/dm<sup>3</sup> (>160 mW/in<sup>3</sup>) is required for the desired application(s) on a wagon. Furthermore, the above-mentioned upper limit for power density is for a high vibration acceleration (5 g) and frequency (38 Hz), which is already on the mechanical limit of the specific harvester [6].

Hence, a different auxiliary energy supply system for a freight wagon, which combines the advantage of an axle generator (high-power density) with the advantage of established EH systems (non-invasive extraction, ease of installing/to retrofit), is required and presented in this work. A non-invasive kinetic energy recovery system (KERS), with an output power in the watt range, is analysed in a case study for a freight wagon. It fills the gap concerning power delivering capability between traditional EH systems (milliwatt range) and axle generators (kW range). The extraction is performed electromechanically from a surface of a wagon's wheel, denoted as moving conductive surface (MCS) in the following. The application scenario at hand is depicted in Fig. 1a.

To guarantee a reliable operation of the KERS, the extraction is performed in a contactless/non-invasive manner; hence, an electromagnetic interaction between the system and the MCS is utilised. In the considered freight train application, the train wheel, i.e. the MCS, is typically made of the non-hardened structural steel of high carbon content (0.4–0.6%) with a tensile strength of ~880 N/mm<sup>2</sup> [7]. Harvesting from the rails, which are typically made of steel with higher carbon content (0.6–0.8%) and a typical tensile strength of 1050 N/mm<sup>2</sup>, would be another option [7].

To define the specifications toward reliability further, an air gap of 10 mm between the MCS and the KERS is mandatory to allow encapsulating the system and for providing free space that is necessary due to vibrations and geometric tolerances. Systems capable of extracting power from linear motion of a solid conductive body are presented and/or analysed in [8–13]. We have discussed a concept [9, 14], which utilises a linear stator and the MCS as a secondary, from which energy is extracted. However, the achievable air gap is limited to only  $\approx 1.5$  mm for a reasonably

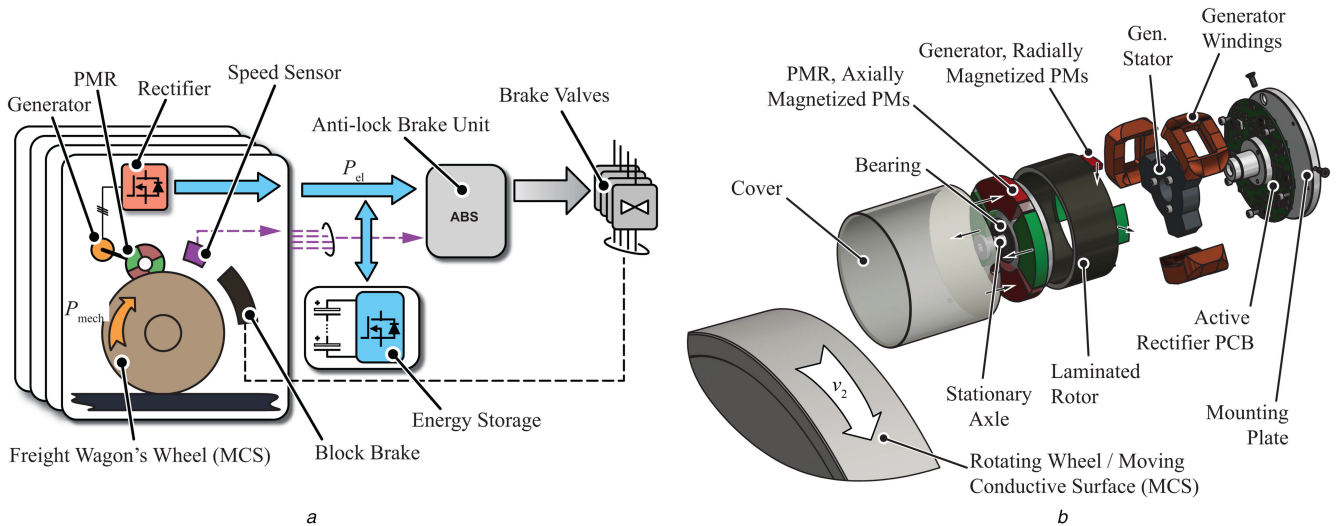


**Fig. 1** Application of the proposed KERS system and its components

(a) KERS system (comprising a PMR a generator, and an active rectifier unit for generating a DC-output voltage) in an application on a wagon of a commercial freight train. Watt-range power is directly extracted onboard the wagon in a non-invasive way so that, e.g. an anti-lock braking system can be supplied for each of the wheel sets, (b) Exploded assembly drawing of the system with PMR, the integrated generator and the active rectifier unit generating a stabilised DC-output voltage

**Table 1** System requirements

Parameter	Variable	Value
MCS speed	$v_2$	80 km/h
air-gap width	$g$	10 mm
output power	$P_{DC}$	>5 W

sized system. Units presented in [8, 10, 11] utilise radially magnetised permanent magnets (PMs) for at first extracting kinetic energy over an air gap and then converting it into electric energy. The latter step can be performed either by additional coils around the harvester wheel or by an additional generator. Similar to [9, 14], the air gap for a watt-range EH system is limited to the lower millimetre range (Table 1).

To overcome the above-mentioned limitations, an improved system, which is illustrated and characterised in Fig. 1b is utilised. It comprises of:

- a rotor with axially magnetised PM rotor (PMR), which extracts/recovers energy from the movement of an MCS (with a nominal surface velocity of  $v_2 = 80$  km/h) over an air gap of  $g = 10$  mm;
- an optimised generator, which is designed as an outrunner and utilises radially magnetised PMs in a pot-shaped rotor; and
- an integrated active rectifier, which rectifies the generator's AC voltages/currents and delivers electric power to a DC output with a nominal voltage of  $U_{DC} = 24$  V.

Furthermore, the system can be encapsulated, such that it is robust against environmental impacts such as dust. The system is built considering a nominal electric output power of >5 W as required for the supply of an anti-lock braking unit including the actuation of the braking valves.

Although the integration of energy storage is not within the scope of this paper, it should be noted that such storage would allow buffering the electric power in case of lower train speed or high-power demand from the actuator system. This would allow designing the KERS for the average power (instead of peak power) demand and accordingly smaller.

In [12], we have introduced a system with axially magnetised PMs, which is capable of extracting watt-range energy over an air gap of 8 mm. However, only the energy extraction from a non-ferromagnetic (aluminium) wheel as MCS has been analysed. In this paper, the research path is continued and utilising an improved KERS on a freight train is discussed as a case study, modelled analytically and analysed with measurements. As detailed in Section 3, an optimised generator is necessary for ensuring the self-start-up of the KERS at hand. We detailed this optimisation in [13],

while only initial measurement results, which were necessary for justifying the therein shown generator optimisation, were given.

This work extends initial findings of [12, 13] with demonstrating the system's suitability as an auxiliary power supply for a freight wagon. The case study is backed up with an analytical model, introduced in Section 2, which explains the energy transfer efficiency and the robustness of in-plane mounting error (overlap length  $l_{ov}$ ) accurately. Subsequently, also an active rectifier is integrated into the KERS and details are given in Section 4. Section 5 details test results, the utilised test setup and verifies the analytical model. Measurement series, which show the influence of key operating parameters, e.g. the MCS-PMR overlap ( $l_{ov}$ ), MCS speed ( $v_2$ ) and the air-gap width ( $g$ ) are given. This paper gives an economic investigation with modelling the additional energy consumption of a KERS on a wagon in Section 6. An efficiency comparison with a possible alternative system is given as well. Finally, conclusions are drawn in Section 7.

## 2 Electromechanical interaction of PMR and MCS

Eddy-current couplings are mature technology [15–18]. They are typically utilised in heavy-duty drivetrains for overload protection and vibration isolation [19] as they are characterised by low maintenance requirements [20]. The functional principle of the PMR-MCS interaction is illustrated in Fig. 2. It is similar to an axial-flux eddy-current coupling. However, in standard eddy-current couplings, the two shafts are coaxial in order to maximise the coupling efficiency [21]. On the other hand, such a coaxial arrangement is not suitable in the case at hand, as it would rigorously limit the mounting flexibility.

### 2.1 Aluminium MCS

Computationally efficient analytical models, which solve Maxwell's equations for coaxial eddy-current couplings, as, e.g. discussed in [22], cannot be derived for the PMR due to missing symmetry properties. Finite element method (FEM) simulations, which calculate the volumetric Lorentz force density

$$f_{\text{Lorentz}} = \mathbf{j} \times \mathbf{B}, \quad (1)$$

where  $\mathbf{j}$  is the eddy-current density and  $\mathbf{B}$  is the magnetic flux density, are an adequate tool for modelling the PMR's performance in case of an aluminium (i.e. non-ferromagnetic) MCS. The arrangement of [12] with disc-shaped, axially magnetised PMs and an aluminium MCS is considered here for illustrative purposes. The MCS wheel has a diameter of 200 mm, 45 mm axial length and 15 mm thickness. Moreover, the conductivity of aluminium is

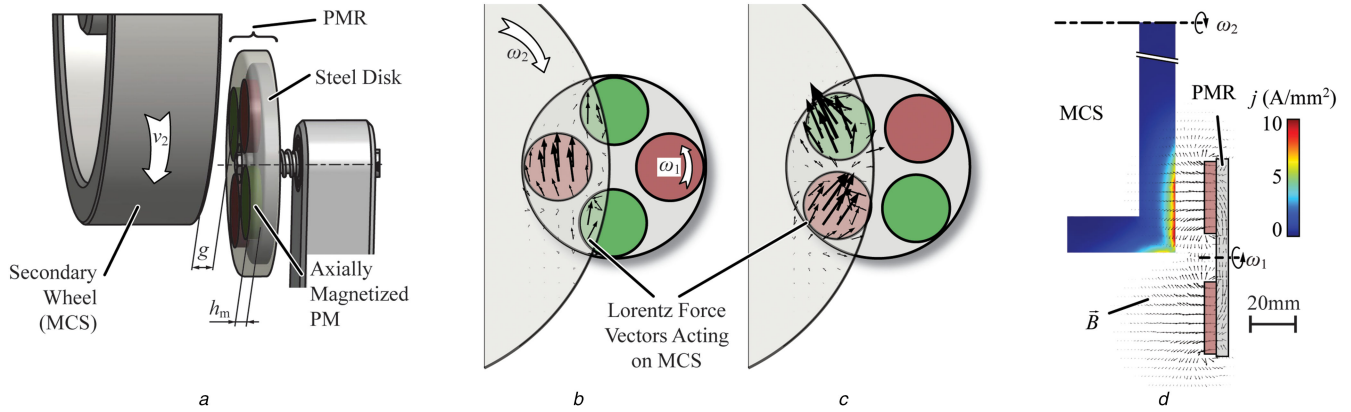


**Fig. 2** System illustration, comprising a PMR with axially magnetised PMs and an iron yoke, rotating in close vicinity of a rotating aluminium wheel (i.e. an MCS) [12]. Kinetic power is transferred electromechanically over an air gap  $g$  between MCS and PMR

(a) Side view of the system, illustrating the air gap ( $g$ ) and the PM height ( $h_m$ ). The built-up Lorentz forces in the MCS are depicted for two different PMR positions in (b) and (c) with black arrows as a result of a 3D FEM simulation. In, (b) A large fraction of the Lorentz force contributes to the torque of the PMR. Although in, (c) the Lorentz force magnitudes are higher, the torque of the PMR is diminished due to their directions. A cross-sectional view of a 3D FEM simulation in, (d) Illustrates the induced eddy currents

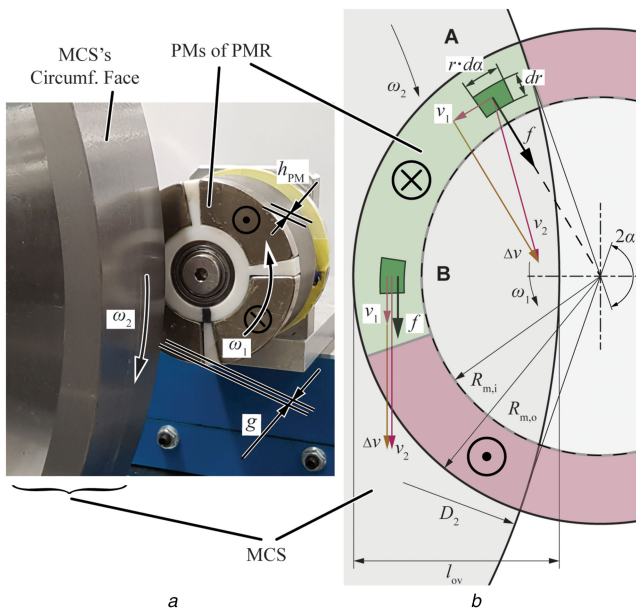


**Fig. 3** Illustration of force generation

(a) Geometric arrangement of the PMR relative to the MCS, (b) Illustration of built-up forces. When a PM is in position A, the force  $F$  acting on it does not create a torque of the PMR. When a PM is in position B, the complete force acting of the PM contributes to a torque on the PMR

set to  $\kappa_{Al} = 28 \text{ MS/m}$  and the PMs have a remanent flux density of  $B_r = 1.4 \text{ T}$ .

Figs. 2b and c show the build-up of Lorentz force for two different rotational positions of the PMR. A difference in speeds of the magnets and the MCS leads to induced eddy currents, and consequently to the build-up of Lorentz force.

Unlike in the case of wound or cage rotors of conventional induction machines, separate guides for flux and current (i.e. teeth made of magnetic steel and copper or aluminium conductors in slots therein) do not exist in the utilised setup. In Fig. 2d, a cross-sectional view of PM flux and currents induced in the MCS is depicted. It can be seen that currents are mainly induced in a skin depth in the millimetre range.

## 2.2 Realised PMR with steel MCS

To achieve a higher-power density of the PMR, the circular magnets of [12] (compare Fig. 2) are replaced by sector-shaped magnets in the case at hand. Fig. 3a shows the realised PMR facing an MCS with a 450 mm diameter. Further dimensions and specifications are given in Fig. 3 and Table 2, respectively.

**Table 2** EH system specifications; geometric dimensions according to Fig. 3

Parameter	Variable	Value
magnet inner radius	$R_{m,i}$	20 mm
magnet outer radius	$R_{m,o}$	38.5 mm
radius of the MCS	$D_2$	450 mm
magnet height	$h_{PM}$	9 mm
magnetic pole pairs of PMR	$p_1$	2
PM grade	—	N48M
PM remanence	$B_r$	1.4 T
PM permeability	$\mu_{PM,rel}$	1.05
nominal OP	—	—
overlap	$l_{ov}$	27 mm
air gap	$g$	10 mm
MCS rotational Speed	$\omega_2$	98.8 rad/s

Fig. 4a shows measurements of input and output power, characterising the kinetic power transfer from the MCS to the PMR. Power transfer from an aluminium MCS (Ac-112, Mat. No. 6082, compare [23]) of same dimensions (compare Table 2) can be described well with a linear increase in torque with increasing slip between the PMR and the MCS (compare ‘o’ markers in Fig. 4a). This characteristic is essentially the same as the torque–speed characteristic of a squirrel-cage induction machine in the region between zero slip and breakdown torque point.

However, on a freight wagon, the KERS has to extract/recover power from a steel wheel. Therefore, in a next step an MCS made of C45E (Mat. No. 1.1191, compare [24]) steel, which has similar physical properties and metallurgic composition to steels used worldwide for freight train wheels [7], is used for the further analysis. Steel C45E is ferromagnetic and shows a comparably large hysteresis (compare Fig. 5). Hence, it can be expected that a power transfer is slightly different from the case with aluminium MCS.

When loading the PMR, only discrete operating points (OPs) are apparent (compare ‘x’ markers in Fig. 4a). Each OP corresponds to a magnetisation pattern on the MCS. The pattern has an even number of poles and is affected by the PMs of the PMR. It is retained due to the steel's remanence and partly residual eddy currents. The magnetic field on the MCS was measured during the operation (at a sufficient distance from the PMR) using a Teslameter ‘Wuntronic KOSHAVA5’ and results are shown in Fig. 4b. The shown duration equates to one revolution of the MCS with  $\omega_2 = 98.8 \text{ rad/s}$ . When operating the PMR with  $\omega_1 \approx 2\omega_2$ , four pole pairs appear on the MCS (compare Fig. 4b left). With higher speeds, a different number of pole pairs appear according to

$$p_2 = p_1 \cdot \left[ \frac{\omega_1}{\omega_2} \right]. \quad (2)$$

The measured remanent magnetic field shows an amplitude of  $\approx 0.5$  mT, which indicates that a magnetic interference with the environment is unlikely.

Concerning the modelling of this KERS operating with steel MCS:

- the skin depth and, hence, a desired mesh size of the MCS is by a factor of

$$\sqrt{\frac{\mu_{\text{rel, C45E}} \cdot \kappa_{\text{FE}}}{\kappa_{\text{Al}}}} \approx 10$$

smaller than with an aluminium MCS and

- for an accurate FEM modelling of the system the effect of remanent magnetism, as shown in Fig. 4b, has to be taken into account as well.

It should be noted that the smaller skin depth leads to an increased required number of mesh elements in the MCS. It ranges between  $10^2$  (refined only on the surface) and  $10^3$  (refined mesh all over the wheel body), as the surface of the MCS and a sufficiently thick layer under the surface are desirable to have a finer mesh.

Additionally, simulating remanent magnetism is currently either not implementable with commercially available magnetic time-

transient three-dimensional (3D) FEM simulation tools or it leads to unreasonably high simulation times. As both of the above-mentioned points lead to the unreasonably high computational effort, an analytical model, which describes the electromechanical power transfer based on geometric analysis, is described as follows.

### 2.3 Analytical model for power transfer

For an infinitesimal intersection area (compare Fig. 3b), the build-up force on the MCS shall be assumed to be in-line and proportional to the speed difference of PM and the MCS

$$-f = k_F \cdot (v_1 - v_2), \quad (3)$$

where  $v_1$  and  $v_2$  are the speeds of the PM and MCS with respect to a stationary observer. The scaling parameter  $k_F$  depends on the geometry and positioning of the PM, as well as on material parameters. The force that is built-up on the PM (while passing over the MCS) can also be calculated from (3) as it is the reaction force  $f$ , pointing in reverse direction. Forces generated at two PM positions are illustrated in Fig. 3b. In position A, a force  $f$  is built-up but does not contribute to the torque acting on the PMR, as it points toward the rotational centre of the PMR. On the other hand, in position B, the complete force acting on the PM accounts for PMR torque generation. In both positions, the force acting on the MCS generates a braking torque. According to Fig. 3, the overlap

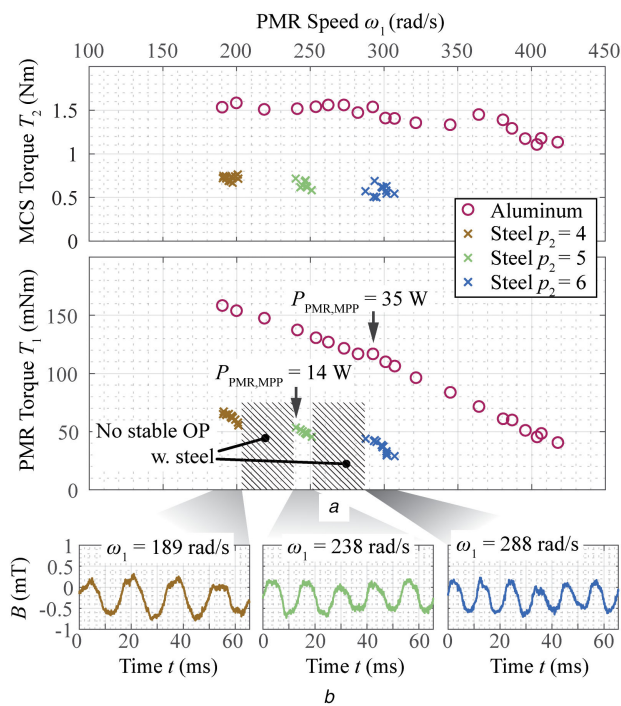


**Fig. 4** Realisation and measurements

(a) Harvested torque  $T_1$  and input torque  $T_2$  over a range of values of the EH rotational speed  $\omega_2$ . Owing to a partial magnetisation of the steel wheel, i.e. the MCS, synchronous operating modes are occurring, (b) Measured remanent magnetisation on the circumferential surface of the C45E steel wheel. The shown duration in time equates to one revolution of the steel wheel, (c) Disassembly of the proposed EH system, (d) Harvester system with outer dimensions. Wires on the right are for extracting the DC-output voltage/power

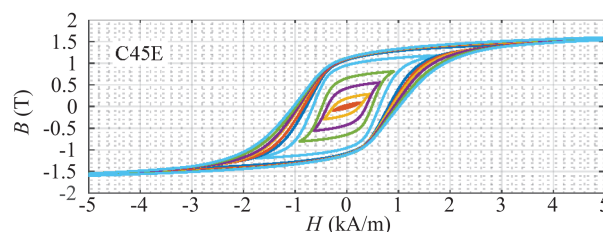


**Fig. 5** Hysteresis curves of steel C45E used for the wheel (compare [25]) at the excitation frequency of 1 Hz

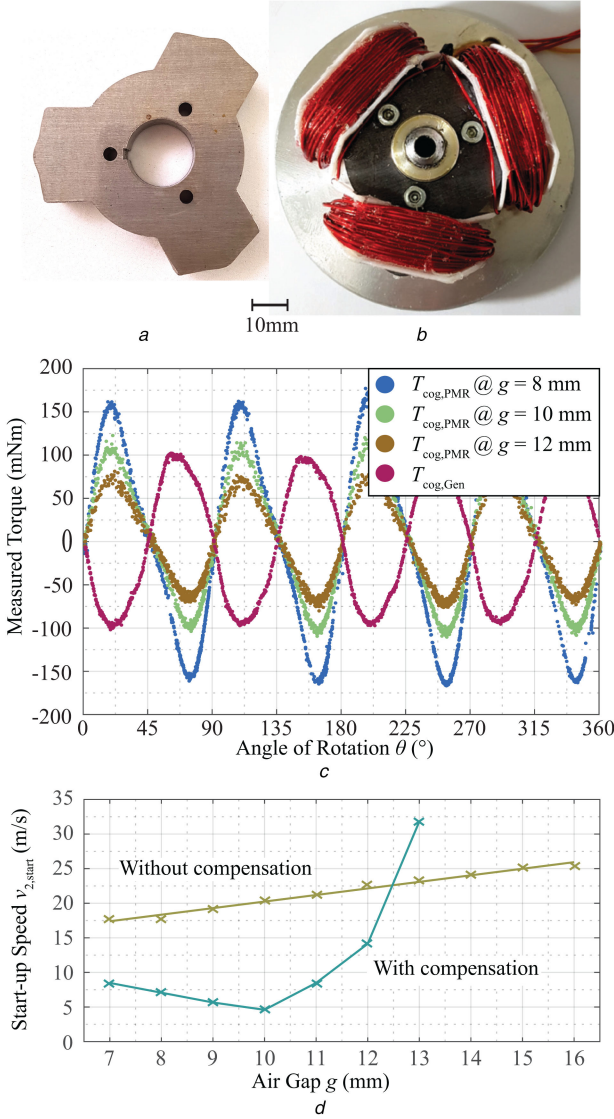


**Fig. 6** Generator and measurements

(a) Picture of the optimised stator. The algorithm that is detailed in [13] has been applied, (b) Generator with wound coils, (c) Plot of measured cogging torque of the PMR–MCS pair with three different air-gap widths and measured cogging torque of the generator, (d) Reduction of start-up speed due to a cogging torque compensation [13]

$l_{\text{ov}}$  is a key operating parameter and has to be adjusted, such that optimal performance can be achieved.

The effect of the circumferential surface of the conductive body, which is, as can be seen from Fig. 3, just in front of the disc with magnets is neglected in (3). Moreover, (3) does not model magnetic remanence nor does it model the distribution of magnetic fields and induced currents as it could be obtained by solving Maxwell's equations. Nevertheless, as confirmed later in this work, (3) can accurately model the optimal adjustment of the overlap  $l_{\text{ov}}$  and the efficiency of the electromechanical power transfer  $\eta_{\text{PMR}}$ .

The velocity of all points on the surfaces of the PMR's PMs (subscript 1) and on the MCS (subscript 2) can be expressed as

$$\mathbf{v}_i = \boldsymbol{\omega}_i \times \mathbf{r}_i, \quad (4)$$

where  $\mathbf{r}_i$  are the vectors pointing from each centre of rotation to a point of interest.

A force acting on a point can be calculated from (3). Similarly, a torque can be obtained. By integrating the torque contributions over the overlapping surface, the total torque on PMR and MCS, respectively, can be calculated as

$$\mathbf{T}_i = \int \int \mathbf{r}_i \times \mathbf{f}. \quad (5)$$

Furthermore, this calculation is conducted in a cylindrical coordinate system as

$$\mathbf{T}_i = \int_{R_{m,i}}^{R_{m,o}} \int_{\pi-\alpha}^{\pi+\alpha} \mathbf{r}_i \times \mathbf{f} \cdot r_1 \, d\alpha \, dr, \quad (6)$$

where the used symbols are in accordance with Fig. 3b.

The analytical expressions for the torque on the PMR

$$\begin{aligned} T_1 = & -\frac{k_F}{6} \cdot (3(\omega_1 + \omega_2)(R_{m,o}^4 - R_{m,i}^4) \cdot \gamma_1 \\ & - 2\omega_2 \frac{(R_{m,o}^3 - R_{m,i}^3)}{R_{m,o}} \gamma_2) \end{aligned} \quad (7)$$

and for the torque of the MCS

$$\begin{aligned} T_2 = & \frac{k_F}{6} \cdot (3(R_{m,o}^2 - R_{m,i}^2) \\ & \cdot [\omega_2(2l_{\text{ov}}^2 + 2r_2^2 + 4r_2R_{m,o} + 3R_{m,o}^2 - 4l_{\text{ov}}(r_2 + R_{m,o})) \\ & + \omega_1 R_{m,o}^2 + (\omega_1 + \omega_2)R_{m,i}^2] \cdot \gamma_1 \\ & - 2(\omega_1 + 2\omega_2) \frac{(R_{m,o}^3 - R_{m,i}^3)}{R_{m,o}} \cdot \gamma_2) \end{aligned} \quad (8)$$

$$\gamma_1 = \text{Cos}^{-1} \left[ \frac{2(r_2 + R_{m,o})(R_{m,o} - l_{\text{ov}}) + l_{\text{ov}}^2}{2R_{m,o}(r_2 + R_{m,o} - l_{\text{ov}})} \right] \quad (9a)$$

$$\gamma_2 = \sqrt{l_{\text{ov}}(2r_2 - l_{\text{ov}})(2R_{m,o} - l_{\text{ov}})(2r_2 + R_{m,o} - l_{\text{ov}})}, \quad (9b)$$

as functions of geometric parameters (the overlap  $l_{\text{ov}}$  and rotational speeds  $\omega_1$  and  $\omega_2$ ) can be obtained by integrating (6) in the given boundaries.

The power  $P_{\text{PMR}}$ , which is transferred from the MCS to the PMR, and mechanical power  $P_2$ , which is supplied from an actuator that spins the MCS (not shown in previous figures), can be calculated as

$$P_{\text{PMR}} = T_1 \cdot \omega_1, \quad (10a)$$

$$P_2 = T_2 \cdot \omega_2, \quad (10b)$$

$$\eta_{\text{PMR}} = \frac{P_{\text{bluePMR}}}{P_2}. \quad (10c)$$

Similarly to scaling laws described in the literatures [9, 26, 27], the scaling parameter  $k_F$  of (3), (7) and (8) can be obtained by a single measurement or FEM simulation. Nevertheless, the main focus of the described model is on efficiency results and the influence of overlap length  $l_{\text{ov}}$  with regard to the maximum power point (MPP), which are independent of  $k_F$ .

### 3 Self-start-up and generator design

Clearly, after kinetic energy is extracted/recovered from the MCS, the mechanical power has to be converted into electric power using a generator. To obtain a compact EH prototype (compare Figs. 4c and d), a generator, which beneficially utilises the confined space is designed. The generator is a brushless DC (BLDC) outrunner machine with concentrated windings. The stator is depicted in Figs. 6a and b.

When operating the proposed KERS with a ferromagnetic steel wheel as MCS, it can be found that at the standstill, the PMs of the PMR tend to align in an energetically optimal position with the wheel. Accordingly, a cogging torque on the PMR occurs (compare Fig. 6c). Thus, a self-start-up of the KERS can only be achieved with relatively high MCS speed  $v_2$ . To achieve a self-start-up at

much lower MCS speeds, the cogging torque of the PMR is compensated with a counter cogging torque introduced by an optimised generator. Measured cogging torque curves of the generator and the PMR for three different air-gap positions are shown in Fig. 6c. A stator optimisation algorithm for obtaining the specially shaped counter cogging torque of the generator is described in [13]. Finally, the compensation of the cogging torque

results in a significantly improved start-up performance, characterised in Fig. 6d with a reduction of the start-up speed from  $v_2 = 20$  to 5 m/s for the nominal air-gap width  $g = 10$  mm.

#### 4 Design of power electronics

Besides the generator, the rectifier stage is also integrated into the KERS. The compact arrangement of the active rectifier has a ring-shaped form factor (compare Fig. 7a) that allows a mounting between the generator and the mounting plate (compare Fig. 1b). The pulse-width modulated (PWM) rectifier is implemented in a six-switch two-level configuration as the schematic representation in Fig. 7b shows. In the design process, special care was taken about utilising low-power components for analogue measurement processing and an ultra-low-power microcontroller STM32L476 is used for the digital control of the system. Furthermore, integrated 80 V gallium nitride half bridges TI LMG5200 are used for each bridge leg, which further contributed to the feasibility of integrating the rectifier in the EH unit. In total, no-load losses of 0.2 W were measured. These include:

- the auxiliary power supply losses and losses in a conversion from  $U_{DC} = 24$  V down to voltage levels that are required for signal electronics and the microcontroller;
- losses of all signal electronics, gate drives and analogue measurement processing including a shunt-type output current measurement; and
- losses in the microcontroller.

The efficiency of the active rectifier, measured for typical OPs that occur during the EH operation, is shown in Fig. 8a. Efficiency measurements (and all further presented electric-power measurements) were conducted with a 'YOKOGAWA WT3000' precision power analyser.

The control of the generator was implemented in a sensorless manner [28] with a BLDC control scheme, which is state-of-the-art for PM synchronous machines in the 10 W power range. Measurements of the resulting block-shaped currents are shown in Fig. 8b for the nominal OP according to Table 2.

The control strategy for the DC-link voltage is implemented with a proportional controller as

$$i_{BLDC, ref} = K_p \cdot (24 \text{ V} - U_{DC, meas}), \quad (11)$$

where  $i_{BLDC, ref}$  is the current reference for the BLDC current in the generator and  $K_p$  is the proportional gain.

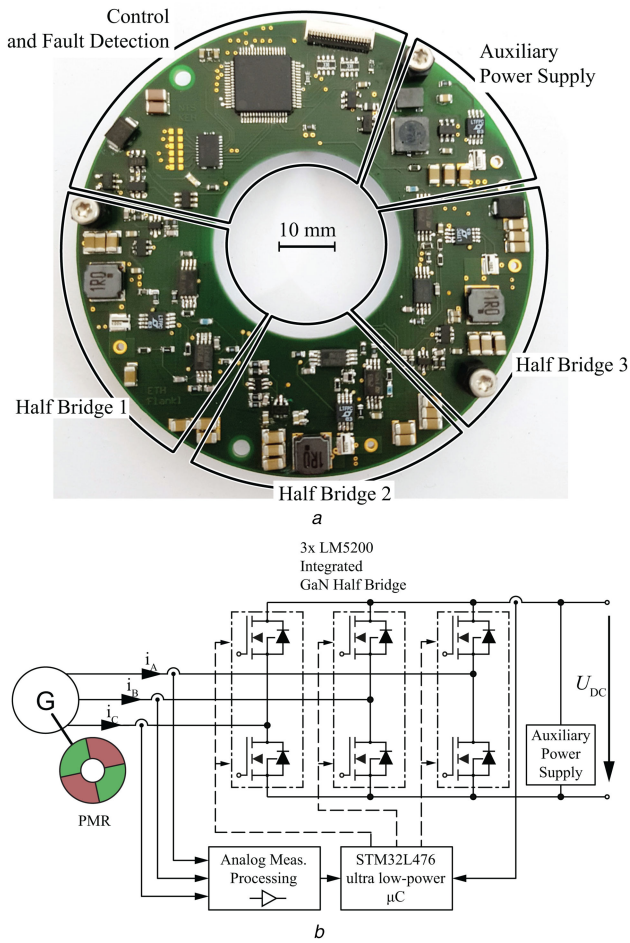


**Fig. 7** Rectifier and schematic representation

(a) PWM rectifier printed circuit board with three half bridges, the auxiliary power supply and the digital control implemented on an ultra-low-power microcontroller STM32L476, (b) Schematic representation of the EH system

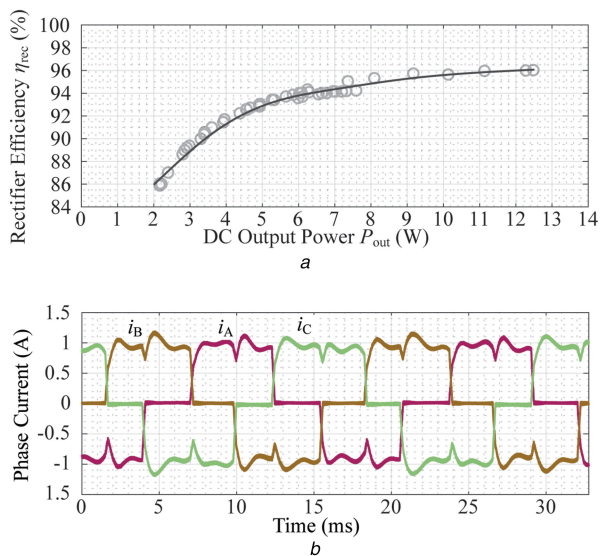


**Fig. 8** Rectifier efficiency, current waveforms and test setup

(a) Measured efficiency of the active rectifier, (b) Measured block-shaped phase currents, (c) Test setup used for measuring the performance of the EH system. An induction machine is used to drive the test wheel (MCS) and a torque sensor is used for measuring a mechanical input power

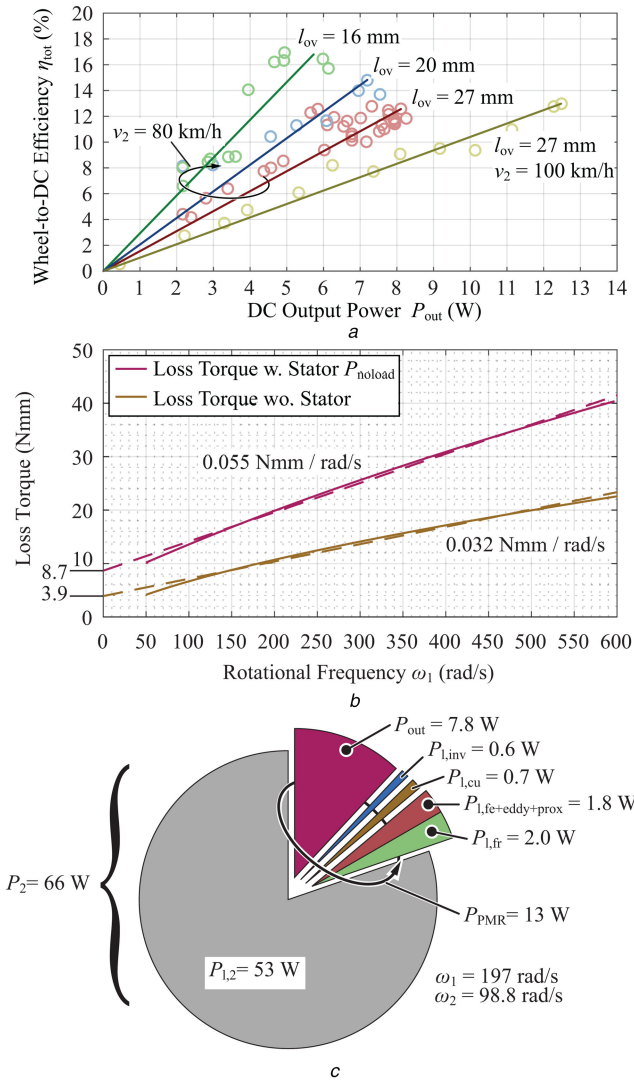


**Fig. 9** Measurements on KERS efficiency and friction losses  
 (a) Overall efficiency versus DC-output power for the C45E steel MCS. Air gap was set to  $g = 10\text{mm}$ , (b) Friction and eddy-current losses (of the EH system) obtained by a run-down measurement, (c) Loss diagram for the nominal OP of the EH with the steel wheel.  $P_{l,2}$  are losses in the steel wheel, i.e. the MCS,  $P_{l,fr}$  are the losses in the PMR's bearings,  $P_{l,fe+eddy+prox}$  are the losses in the PMR's iron (of the generator), eddy-current losses and proximity losses.  $P_{l,cu}$  are generator copper losses and  $P_{l,inv}$  losses in the active rectifier including all signal electronics.  $P_{out}$  is the DC-output power available on the system's clamps

## 5 Test setup and measurement results

Measurements of the system were conducted with the test setup as shown in Fig. 8c. An induction machine with a commercial variable speed machine drive is driving the MCS, which acts as a mock-up of a train wheel. Owing to practical limitations, the wheel has a diameter of  $D_2 = 450\text{mm}$ , which is approximately half the diameter of an actual train wheel. A mounting system on the interface drive shaft and the wheel allows to change the wheel, and hence testing the system with different MCS materials. A torque sensor (type Burster 8661-5050-1210 with  $\pm 10\text{mNm}$  accuracy) on the driving shaft allows measuring the mechanical input power. The KERS is mounted on a positioning stage, which allows adjustments of the air gap  $g$  and overlap  $l_{ov}$ .

Fig. 9a shows output power measurements for different OPs (in terms of the overlap and speed) when the DC output of the system is gradually loaded with a resistive load. On the vertical axis, the total (i.e. wheel-to-DC) efficiency  $\eta_{tot}$  is depicted, where the input power was measured with the torque sensor and the output power with the power analyser. Owing to the previously described effect of remanent magnetisation of the steel wheel, the measurement points tend to spread slightly.

For a detailed investigation of losses, the bearing friction losses in the KERS (one SKF 608-2Z and one SKF 609-2Z deep groove ball bearings are utilised to support the rotor) and the generator iron and proximity losses were measured accumulatively in a run-down test. Therefore, the system's moment of inertia (around its rotational axis) is calculated at first. Afterwards, the machine/generator/system is accelerated to a rated speed in an experiment and its deceleration is recorded. One can subsequently calculate the loss torque using the rotational form of Newton's second law. The measurement results and a fitted model are given in Fig. 9b.

In the following, the electromechanically extracted power is calculated from the measured electrical quantities. Therefore, copper losses and measured no-load losses of Fig. 9b were added to the measured electric generator output power

$$P_{KERS} = P_A + P_B + P_C + R_{gen} \cdot (I_A^2 + I_B^2 + I_C^2) + P_{no\ load}, \quad (12)$$

where  $P_{no\ load}$  are the no-load losses according to the model of Fig. 9b. It should be stated that the earlier presented results depicted in Fig. 4a were obtained with the same method.

A distribution of losses for the nominal OP can be found in the illustration of Fig. 9c. Most losses occur in the MCS due to the non-coaxial interaction with the PMs. Losses due to bearing friction and iron losses are relevant as well, while copper losses and losses in the power electronics are insignificant.

### 5.1 Overlap trade-off

Fig. 10a shows results, which illustrate a trade-off in choosing the overlap length  $l_{ov}$ . A higher overlap leads to increased coupling between PMR and MCS, but also to higher losses. Therefore, electromechanically extracted power and the respective efficiency are plotted. Besides the measurement results, the results of the analytical model derived in Section 2.3 [in specific (7), (8) and (10)], are shown in Fig. 10a.

The PMR input power was calculated according to (12), such that in Fig. 10a measurement results can be compared with results that are predicted by the analytical model (of Section 2.3). For each fixed value of the overlap length ( $l_{ov}$ ), a variety of OPs, in terms of different load conditions, can be reached. Results for the MPP are plotted in Fig. 10a. Analytical model and measurement results agree very well for the efficiency plot in Fig. 10a. For the diagram of extracted power in the lower plot of Fig. 10a, the power scaling constant required for the analytical model is set to  $k_F = 175\text{Ns/m}^3$ . A limitation of the analytical model can be found when the overlap is smaller than the radial width of the PMs  $l_{ov} < R_{m,o} - R_{m,i} = 18.5\text{mm}$ . The analytical model overestimates the extracted power in this region. Nevertheless, it can be concluded that the analytical model predicts the efficiency and the optimal overlap well and/or provides a design guideline.

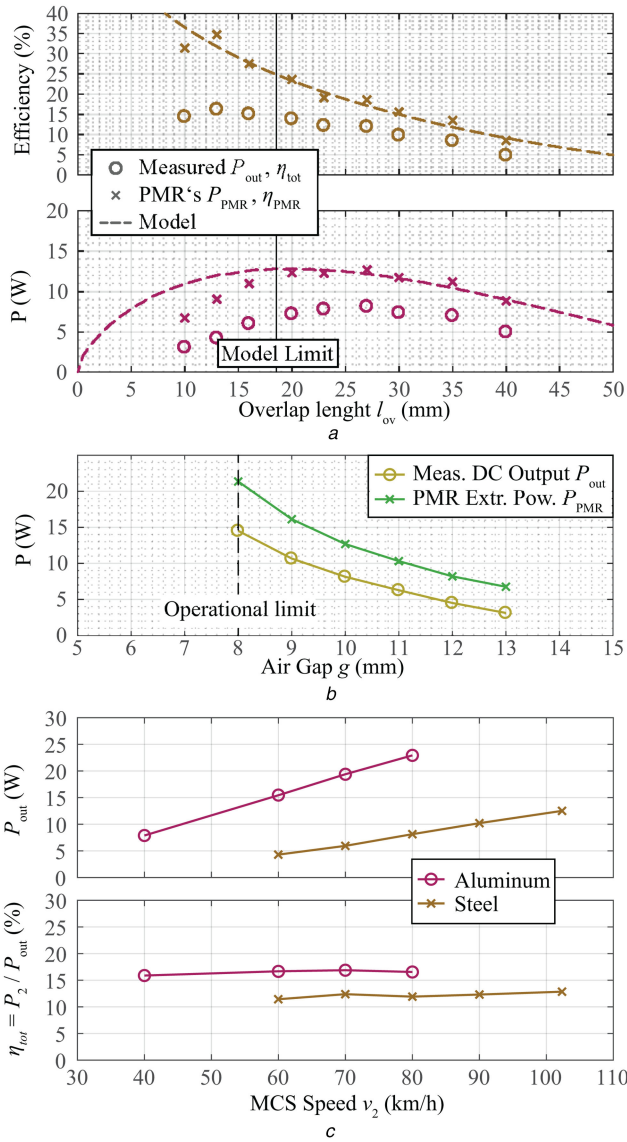
### 5.2 Influence of wheel speed, air gap and wheel material

Fig. 10b shows a decay of extracted power with an increase of the air-gap width  $g$ . This is due to weaker magnetic coupling. It can be seen that the proposed system can deliver the required power of 5 W in the air gap range of  $g = 8 \dots 12\text{mm}$ .

Finally, Fig. 10c shows output power  $P_{out}$  and efficiency  $\eta_{tot}$  measurement results utilising an Ac-112 aluminium wheel and a C45E steel wheel. The extracted power is  $\sim 3$  times higher with the aluminium wheel than with the steel wheel, which can be explained qualitatively due to higher conductivity of aluminium. The couplings' efficiencies are in the same range of  $\eta_{tot} \approx 15\%$ , which agrees with the model of Section 2.3 (Table 3).

## 6 Economy of the non-invasive KERS

In this section, the described energy generation system is evaluated in terms of additional tractive effort for the locomotive and its typical power consumption costs. Moreover, its overall (overhead-



**Fig. 10** Trade-off of operating parameters

(a) Efficiency and output power versus overlap with the steel wheel. The measurements and the analytical models of (7), (8) and (10) are in good agreement. For a small overlap,  $l_{ov} < R_{m,o} - R_{m,i} = 18.5$ mm, the model and measurements diverge as the lower integration boundary of (6) is only correct for a larger overlap, (b) Influence of the air gap on energy extraction. Clearly, extracted power decreases monotonously with increasing air gap, (c) Influence of MCS surface speed (energy recovery source) on the system operation. Extracted power increases with MCS speed, whereas little influence on efficiency can be observed

line-to-low-voltage DC) efficiency is compared with a compressed-air-to-electric-power generation system.

### 6.1 Additional tractive effort

According to Steimel [29], the tractive effort for pulling a typical 4-axle wagon with 88 ton mass at a constant travel speed of 80 km/h on a straight, flat track without tunnels sums up to a mechanical power of  $P_{track, 80} = 40$  kW. According to information received from the railway sector, the average mechanical power demand required to push/pull a freight wagon on a typical drive cycle with slopes, curves and tunnels can be approximated as  $P_{track, avg} = 3 \cdot P_{track, 80} = 120$  kW. Furthermore, it shall be assumed that the PMR is always operating in the MPP with an electrical power output of 7.8 W, leading to a mechanical power demand of  $P_2 = 66$  W (compare Fig. 9c). Therefore, the relative additional mechanical power demand in this scenario is

$$\frac{P_2}{P_{track, avg}} = 0.06\% . \quad (13)$$

**Table 3** Generator parameters

Parameter	Variable	Value
generator phase resistance	$R_{gen}$	$0.437\Omega$
number of pole pairs	$p_{gen}$	2
flux linkage	$\Psi$	0.0156 Wb

### 6.2 Power consumption costs

Moreover, the energy costs of installing the non-invasive KERS on a wagon, which is pulled/pushed by an electric locomotive (as, e.g. in central Europe) shall be analysed. One can assume that a wagon is running 100,000 km per year. According to Steimel [29], the efficiency of a locomotive, powered electrically from an overhead line, can be approximated as  $\eta_{Lok} = 83\%$ . Following the statistical data provided by [30], the electric energy price for a railway company (averaged over Europe and at the overhead line) can be assumed as  $p_{el} = 10$  €Cent/kWh. Therefore, the energy cost per year for installing the KERS on a wagon is

$$C_{KERS} = \frac{100,000 \text{ km/a}}{80 \text{ km/h}} \cdot \frac{1}{\eta_{Lok}} \cdot p_{el} \cdot P_2 = 15 \text{ €/a} . \quad (14)$$

### 6.3 Comparison to an air-to-power system

As above-mentioned in Section 1, a compressed-air-to-electric-power system could theoretically also be considered for generating auxiliary power on a freight wagon. Although such a system could lead to an extensive certification process and/or to a redesign of the compressed-air supply system, it should be considered briefly as follows. It allows comparing the proposed KERS's efficiency to a possible competitor system. A compressed-air-to-electric-power demonstrator system, intended for a non-railway specific application, is shown in [2] and its maximum efficiency was reported as  $\eta_{air2power} = 24\%$ . To compare this approach to the proposed KERS regarding efficiency, total cycle efficiencies must be computed and compared. A chain of all energy conversion stages, starting from the locomotive's DC link over the compressor, the pressurised air pipe system to the wagon has to be considered. According to data available from the industrial sector [31, 32], a typical reciprocating compressor's efficiency including the losses of its electric motor can be assumed as  $\eta_{comp} \approx 50\%$ . Furthermore, the efficiency of the compressor's power supply (from the overhead-line-to-three-phase low-voltage AC) shall be assumed as  $\eta_{aux, pow} = 86\%$  and the average efficiency of the brake pipe system, providing the pressurised air shall be assumed as  $\eta_{pipe} = 85\%$ , considering leakage losses and flow resistance in the pipe. Therefore, total efficiency of the air-to-power system, from the overhead-line-to-power supply on the wagon can be given as

$$\begin{aligned} \eta_{air2power, HV \text{ to } 24 \text{ V}} &= \eta_{aux, pow} \cdot \eta_{comp} \cdot \eta_{pipe} \cdot \eta_{air2power} \\ &= 86\% \cdot 50\% \cdot 85\% \cdot 24\% = 8.8\% . \end{aligned} \quad (15)$$

In comparison, the cycle efficiency of the KERS on a freight train can be given as

$$\eta_{KERS, HV \text{ to } 24 \text{ V}} = \eta_{Lok} \cdot \eta_{PMR, tot} = 83\% \cdot 12\% = 10\% . \quad (16)$$

The obtained overhead-line-to-low-voltage-DC (on the wagon) efficiencies show that both systems are comparable in terms of energy demand and/or efficiency.

## 7 Conclusion

A new type of auxiliary power supply system, suitable for supplying, e.g. an anti-lock braking unit on a freight wagon is presented. The energy source is the motion of the wagon's wheel (i.e. an MCS) and the extraction is conducted non-invasively with a rotor comprising axially magnetised PMs (PMR), forming a KERS. However, the application area is not limited to the railway sector as energy can be extracted from any MCS with sufficient speed.

The presented system allows electromechanical transfer of kinetic energy from the MCS to the PMR in a contactless fashion over a large air gap. Together with a generator and a highly compact PWM rectifier stage, which are both integrated within the KERS, a compact unit with a power density of 22 W/dm<sup>3</sup> (360mW/in<sup>3</sup>) is formed, which is ~20 times higher than power densities of EH systems reported in the literatures [4–6]. An analytical model for estimating the coupling's efficiency and the optimal overlap set point for extracting maximum power is derived analytically and verified with measurements.

As shown in the experiment, the electric power of 7.8 W can be delivered by the proposed KERS at a MCS speed of 80 km/h and an air-gap width of 10 mm. The wheel-to-DC-output efficiency is in the range of 12%. This is well justifiable, given the added benefit of a power supply on a freight wagon and considering the negligible additional power demand of 0.06%.

## 8 References

- [1] Watts, P.H., Hawkrigde, M.S.: 'Mk IV passenger vehicles for east coast main line electrification'. Proc. IEE Conf. Int. Main Line Railway Electrification, York, UK, September 1989, pp. 299–305
- [2] Krähenbühl, D.: 'Bidirectional interfacing of compressed-air and electric power employing ultra-high-speed drives and turbomachinery', PhD dissertation, ETH Zurich, Switzerland, 2010
- [3] Spicer, C.W.: 'Axle generator drive', US Patent US2 026 076A, 10 April 1931
- [4] Khaligh, A., Zeng, P., Zheng, C.: 'Kinetic energy harvesting using piezoelectric and electromagnetic technologies state of the art', *IEEE Trans. Ind. Electron.*, 2010, **57**, (3), pp. 850–860
- [5] Dayal, R., Dwari, S., Parsa, L.: 'A new design for vibration-based electromagnetic energy harvesting systems using coil inductance of microgenerator', *IEEE Trans. Appl. Ind.*, 2011, **47**, (2), pp. 820–830
- [6] Kinergizer, B.V.: 'HiPER-D motion energy harvester datasheet'. Available at <http://kinergizer.com/request-datasheet/>, accessed 11-01-2017
- [7] Mädler, K., Bannasch, M.: 'Materials used for wheels on rolling stock'. Proc. World Congress on Railway Research (WCRR), Montreal, QC, Canada, June 2006
- [8] Strothmann, D.: 'Device for contactless current generation, in particular bicycle dynamo, vehicle lighting system and bicycle', DE Patent WO 2013/004 320 A1, Munich, Germany 10 January 2013
- [9] Flankl, M., Tüysüz, A., de Oliveira Baumann, L., et al.: 'Energy harvesting with single-sided linear induction machines featuring secondary conductive coating', *IEEE Trans. Ind. Electron.*, 2019, **66**, (6), pp. 4880–4890
- [10] Magnic Innovations GmbH & Co KG.. Available at <http://www.magniclight.com>, accessed: 28-11-2017
- [11] Shun-Fu Technology Corp.: 'Induktions generator', DE Gebrauchsmuster DE 202 014 100 380 U1, 24 04 2014
- [12] Flankl, M., Tüysüz, A., Subotic, I., et al.: 'Novel contactless axial-flux permanent-magnet electromechanical energy harvester'. Proc. Applied Power Electronics Conf. Expo. (APEC), Long Beach, CA, USA, March 2016
- [13] Flankl, M., Tüysüz, A., Kolar, J.W.: 'Cogging torque shape optimization of an integrated generator for electromechanical energy harvesting', *IEEE Trans. Ind. Electron.*, 2017, **64**, (12), pp. 9806–9814
- [14] Flankl, M., Tüysüz, A., Kolar, J.W.: 'Analysis and power scaling of a single-sided linear induction machine for energy harvesting'. Proc. IEEE Industrial Electronics Conf. (IECON), Yokohama, Japan, November 2015
- [15] Davies, E.J.: 'General theory of eddy-current couplings and brakes', *Proc. IEEE*, 1966, **113**, (5), pp. 825–837
- [16] Davies, E.J., James, B., Wright, M.T.: 'Experimental verification of the generalised theory of eddy-current couplings', *Proc. IEEE*, 1975, **122**, (1), pp. 67–72
- [17] Davies, E.J.: 'An experimental and theoretical study of eddy-current couplings and brakes', *IEEE Trans. Power Appar. Syst.*, 1963, **82**, (67), pp. 401–419
- [18] Bloxham, D.A., Wright, M.T.: 'Eddy-current coupling as an industrial variable-speed drive', *Proc. IEEE*, 1972, **119**, (8), pp. 1149–1154
- [19] Smith, A.C., Willsamson, H., Benhama, N., et al.: 'Magnetic drive couplings'. Proc. IEE Conf. Int. Electrical Machines and Drives, Canterbury, UK, 1999, pp. 232–236
- [20] Erasmus, A.S., Kamper, M.: 'Analysis for design optimisation of double PM-rotor radial flux eddy current couplers'. Proc. IEEE Energy Conversion Conf. Exposition (ECCE-USA), Montreal, QC, Canada, September 2015
- [21] Lubin, T., Rezzoug, A.: '3-D analytical model for axial-flux eddy-current couplings and brakes under steady-state conditions', *IEEE Trans. Magn.*, 2015, **51**, (10), pp. 1–12
- [22] Wang, J., Lin, H., Fang, S., et al.: 'A general analytical model of permanent magnet eddy current couplings', *IEEE Trans. Magn.*, 2014, **50**, (1), pp. 1–9
- [23] European Committee for Standardization.: 'Aluminium and aluminium alloys. Chemical composition and form of wrought products. Chemical composition and form of products', Std. EN 573–3, 2013
- [24] European Committee for Standardization.: 'Steels for quenching and tempering', Std. EN 10 083-1, 2006
- [25] Flankl, M., Tüysüz, A., Kolar, J.W.: 'Impact of iron dust on electromechanical systems: a case study'. Proc. IEEE Southern Power Electronics Conf. (SPEC), Auckland, New Zealand, December 2016
- [26] Soong, W.L.: 'Sizing of electrical machines', *Power Eng. Briefing Note Ser.*, 2008, **9**, pp. 17–18
- [27] Bone, J.C.H.: 'Influence of rotor diameter and length on the rating of induction motors', *IEE Electr. Power Appl.*, 1978, **1**, (1), pp. 2–6
- [28] Kim, K.-H., Youn, M.-J.: 'Performance comparison of PWM inverter and variable DC link inverter schemes for high-speed sensorless control of BLDC motor', *IEE Electron. Lett.*, 2002, **38**, (21), pp. 1294–1295
- [29] Steimel, A.: 'Electric traction: motive power and energy supply' (Deutscher Industrieverlag, Munich, Germany, 2014, 2nd edn.)
- [30] Statistisches Bundesamt (Federal Statistical Office of Germany): 'Preis-Daten zur Energiepreisentwicklung (in German)'. Available at [https://www.destatis.de/DE/Publikationen/Thematisch/Preise/Energiepreise/EnergiepreisentwicklungPDF\\_5619001.pdf](https://www.destatis.de/DE/Publikationen/Thematisch/Preise/Energiepreise/EnergiepreisentwicklungPDF_5619001.pdf), checked 29 March 2018
- [31] Agre Kompressoren GmbH.: 'AGRE industrial piston compressors'. Available at [http://www.hn-druckluft.de/2MARK/1\\_AGRE](http://www.hn-druckluft.de/2MARK/1_AGRE) Kolbenkompressoren MKK MEK MGK Katalog 2017.pdf, checked 29 March 2018
- [32] Schweizerische Agentur für Energieeffizienz.: 'Merkblatt 26: druckluft-kompressoren'. Available at: [https://www.topmotors.ch/sites/default/files/2017-07/26\\_MB\\_Druckluft-Kompressoren.pdf](https://www.topmotors.ch/sites/default/files/2017-07/26_MB_Druckluft-Kompressoren.pdf), checked 29 March 2018